



# Magnetic and structural investigations on $\text{La}_{0.6}\text{Sr}_{0.4}\text{MnO}_3$ nanostructured manganite: Evidence of a ferrimagnetic shell



V.M. Andrade<sup>a</sup>, R.J. Caraballo-Vivas<sup>a</sup>, T. Costas-Soares<sup>a,b</sup>, S.S. Pedro<sup>a</sup>, D.L. Rocco<sup>a,\*</sup>, M.S. Reis<sup>a</sup>, A.P.C. Campos<sup>c</sup>, A.A. Coelho<sup>d</sup>

<sup>a</sup> Instituto de Física, Universidade Federal Fluminense, 24210-340 Niterói, RJ, Brazil

<sup>b</sup> IF Sudeste MG, Campus Juiz de Fora - Núcleo de Física, 36080-001 Juiz de Fora, MG, Brazil

<sup>c</sup> Divisão de Metrologia de Materiais, Instituto Nacional de Metrologia, Qualidade e Tecnologia, 25250-020 Duque de Caxias, RJ, Brazil

<sup>d</sup> Instituto de Física "Gleb Wataghin", Universidade Estadual de Campinas, Caixa Postal 6165, 13083-859 Campinas, SP, Brazil

## ARTICLE INFO

### Article history:

Received 12 May 2014

Received in revised form

11 July 2014

Accepted 12 July 2014

Available online 19 July 2014

### Keywords:

Nanostructured materials

Sol–gel processes

Magnetic measurements

## ABSTRACT

This paper presents the structural and magnetic properties of  $\text{La}_{0.6}\text{Sr}_{0.4}\text{MnO}_3$  nanoparticles with sizes from 21 to 106 nm, which have been prepared using the sol–gel method. The reduction of the nanoparticles' size tends to broaden the paramagnetic to ferromagnetic transition, as well as to promote magnetic hysteresis and a remarkable change on the magnetic saturation. In order to better understand the magnetic behavior of those nanoparticles, a simple model based on a ferromagnetic core and a ferrimagnetic shell was considered, where the magnetization was described in terms of the standard mean-field Brillouin function. This model matches the experimental data, leading to conclusion the nanoparticles with size  $< 40$  nm are single magnetic domain. In addition, the output fitting parameters give information on the Landé factor of the core and shell.

© 2014 Elsevier Inc. All rights reserved.

## 1. Introduction

The physics of nano-materials has been an exciting research field since the 1990s. In particular, magnetic properties have attracted attention not only from a fundamental view but also due to technological applications [1] in medicine [2–4], catalysis processes [5] and magnetic refrigeration [6], for instance. From the fundamental point of view, when the size of the magnetic nanoparticles decreases to a few nanometers the material exhibits different magnetic behaviors, such as surface spin-glass, superparamagnetism, large coercivities, low-field saturation magnetization, and low Curie temperature, as compared to their bulk counterparts [7–10]. These behaviors are mainly due to the particle surface, since its magnetic behavior differs from that corresponding to the core, because of the distinct atomic coordination, compositional gradients and, concentration and nature of the defects present in both regions [11,12]. Thus, the surface gives rise to a large magnetocrystalline anisotropy due to its low symmetry and it also induces the competition between different magnetic arrangements due to weakening of exchange interactions [13].

The manganites with general formula  $RE_{1-x}AE_x\text{MnO}_3$ , where  $RE$  and  $AE$  denote, respectively, trivalent rare-earth and bivalent alkaline-earth elements, have been widely studied due to its special magnetic, thermal and electrical properties [14]. Moreover, these materials exhibit a strong magnetocaloric effect [15] and colossal magnetoresistance [16]. The electric and magnetic properties of these systems are mainly controlled by two factors: the doping level and the average size of the cations placed in the  $A$  site (site shared by  $RE$  and  $AE$ ). The first determines the ratio between  $\text{Mn}^{3+}$  and  $\text{Mn}^{4+}$ , while the second induces a lattice distortion and thus plays a central role on magnetic properties, since the Mn–O–Mn bond is very sensitive to structural changes [17].

Many studies showed that the magnetic properties of manganite nanoparticles obtained by the sol–gel method present novel features compared with the bulk materials, prepared by the conventional solid-state reaction method [18,6]. The observed effects, when the particle size is reduced to few nanometers, are mainly the broadening of the paramagnetic to ferromagnetic transition, decreasing of the saturation magnetization value, increasing of the magnetic hysteresis [19] and appearance of superparamagnetic (SPM) behavior at very low particle size [20] ( $< 17$  nm). In what concerns the magnetocaloric effect, while the decrease of the saturation magnetization is not desired, the broadening of FM-PM transition is considered, sometimes, an advantage due to significant relative cooling power (RCP) [21–23,6]. The lower magnetization of

\* Corresponding author. Tel.: +55 21 26293834.

E-mail address: [rocco@if.uff.br](mailto:rocco@if.uff.br) (D.L. Rocco).

ferromagnetic nanoparticles in comparison to bulk samples is usually explained on the basis of the surface “magnetically dead” layer, whose contribution to the magnetic moment of a nanoparticle is negligible relatively to the magnetic contribution of its core [24,19]. However, the microscopic nature of the surface region is not understood well so far.

In order to further shed light on this issue, we investigated the magnetic properties of  $\text{La}_{0.6}\text{Sr}_{0.4}\text{MnO}_3$  nanoparticles produced by the sol–gel method. The average diameter of nanoparticles ranges from 21 nm to 106 nm, which were determined by X-ray diffraction and confirmed by transmission electron microscopy (TEM). The different features of these nanoparticles were revealed by magnetic measurements, which showed a dependence of the nanoparticle size with magnetic saturation and transition. We developed a theoretical model based on a core(ferromagnetic)–shell(ferrimagnetic) pattern, and an excellent agreement was obtained, leading to conclude that the nanoparticles with size < 40 nm are single magnetic domain. In addition, the output fitting parameters give important information on the Landé factor and critical temperature of the core and shell, as well as define that the ‘magnetically dead’ layer proposed in the literature [24] is, indeed, ferrimagnetic.

## 2. Experimental techniques

Analytical grade  $\text{La}_2\text{O}_3$ ,  $\text{SrCO}_3$  and  $\text{Mn}_2\text{O}_3$  weighted accurately were individually dissolved in nitric and citric acid solution in de-ionized water. The resulting individual solutions were mixed to obtain a clear solution with a molar ratio of La:Sr:Mn = 0.6:0.4:1. A suitable amount of polyethylene glycol was added to the solution, and ethylenediamine was used to adjust the pH value to 8. In order to evaporate the excess of solvents and to promote polymerization, the solution was submitted to 373 K for 6 h and then a yellow transparent viscous solution was obtained, and after 4 h at 373 K the solution becomes highly viscous, changing its color from yellow to brown, and finally it was gelled to a glassy resin. The gel was heated in a furnace for 15 h at 673 K, and a brown precursor was obtained. The powder was divided into four parts and annealed at 973 K, 1073 K, 1173 K and 1273 K for 10 h, and four final black  $\text{La}_{0.6}\text{Sr}_{0.4}\text{MnO}_3$  powders were obtained. The bulk sample was prepared by the conventional solid-state reaction method from stoichiometric amounts of the same starting material cited above. The powders were ground and mixed, then calcined in air at 1373 K for 24 h. The resulting powder was reground, pressed into pellets and then sintered at 1623 K during 36 h.

The magnetic measurements were carried out using a commercial superconducting quantum interference device (SQUID) at Unicamp. X-ray powder diffraction data were obtained at UFF and at room temperature, using a Bruker AXS D8 Advance diffractometer with  $\text{CuK}\alpha$  radiation ( $\lambda = 1.54056 \text{ \AA}$ ), 40 kV and 40 mA. Data were collected in the  $15^\circ < 2\theta < 90^\circ$  range in a Bragg-Brentano geometry, with a step size of  $0.02^\circ$  and a count time of 0.1 s per step. The transmission electron microscopy (TEM) technique was carried out using a FEI-LaB<sub>6</sub>-TECNAL microscope, held at Inmetro, operated at 120 kV, and equipped with a SIS MEGAVIEW III CCD camera. This technique was employed to obtain the bright field (BF) images of the samples, and thus, to prepare a histogram of particle size and analyze its morphology. For these analyses the samples were diluted in alcohol.

## 3. Crystal structure and morphology

The X-ray patterns of the bulk and the samples submitted to calcination temperatures of 973 K, 1073 K, 1173 K and 1273 K

confirmed the formation of a pure  $\text{La}_{0.6}\text{Sr}_{0.4}\text{MnO}_3$  crystalline phase, showing the characteristic peaks of the compound. The diffractograms for all samples can be seen in Fig. 1. The  $\text{La}_{0.6}\text{Sr}_{0.4}\text{MnO}_3$  system presents a perovskite structure at room temperature and pressure, belonging to the space group  $R\bar{3}c$  (group 167) in a rhombohedral crystal system, as reported by Shen [25]. The powder X-ray diffraction data were refined by the Rietveld method using the FullProf software [26]. One example of adjust is shown in the bottom of Fig. 1, for sample calcined at 973 K. The crystallographic parameters and reliability factors obtained from refinement can be seen in Table 1 (only presented for nanoparticles). A pseudo-Voigt (pV) profile function was used to fit the reflection peaks. The convergence factors  $R_p$ ,  $R_{wp}$  and  $R_F$  obtained from the Rietveld analysis point to the good quality of the refinement.

It was possible to estimate the average particle size  $D$  from the powder XRD peaks using the Scherrer equation, which describes the grain size using the size broadening of the peaks from the relation [27]

$$D = k\lambda/\beta_L \cos \theta \quad (1)$$

where  $k$  is a dimensionless constant (close to one),  $\lambda$  is the X-ray wavelength,  $\theta$  is the diffraction angle for the most intense peaks and  $\beta_L = \sqrt{U \tan^2 \theta + V \tan \theta + W}$  is related to the full width at half maximum (FWHM) of the peaks. The broadening of the peaks indicates the formation of a nanocrystalline compound [28,29]. When the calcination temperature arises, the diffraction peaks become sharper, resulting in larger particle sizes [28]. The particle

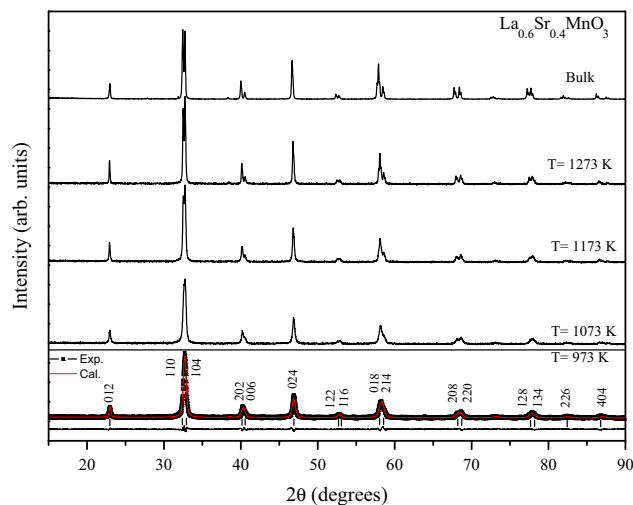
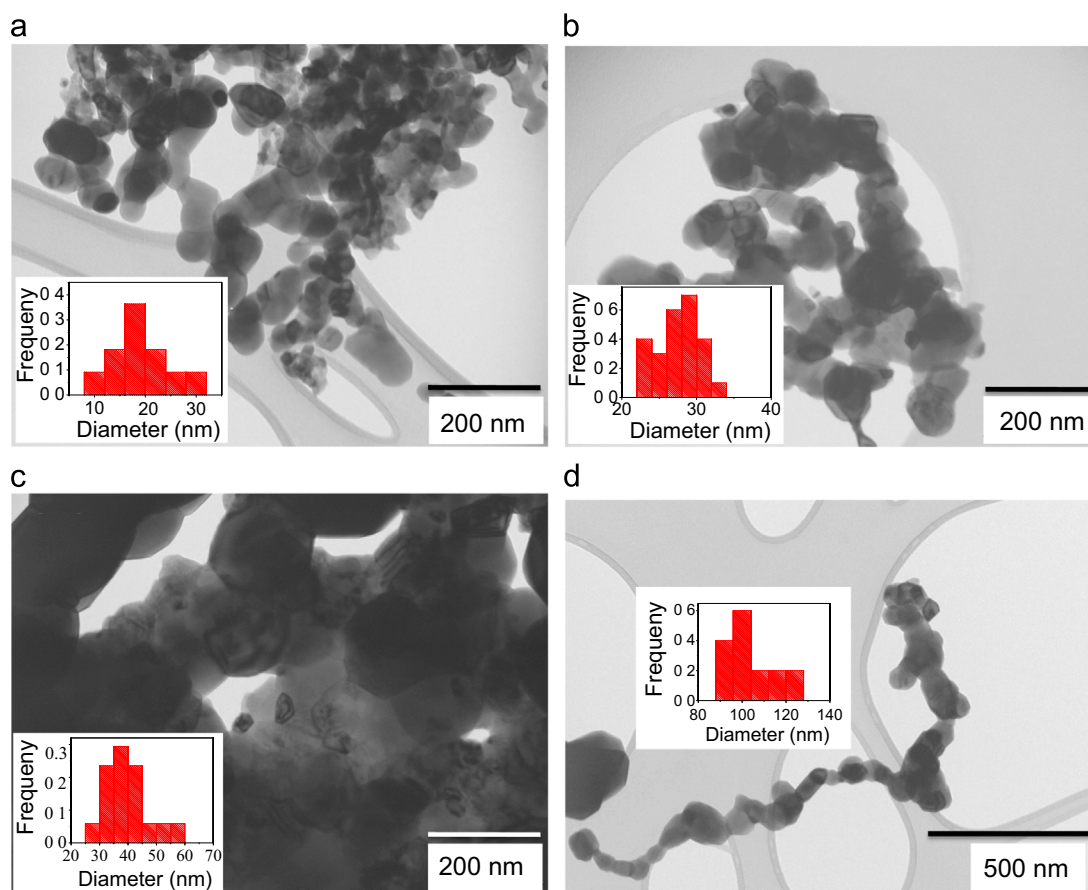


Fig. 1. Powder diffractograms for the  $\text{La}_{0.6}\text{Sr}_{0.4}\text{MnO}_3$  nanoparticles, calcinated at several temperatures. (Bottom) Rietveld refinement for sample calcined at 973 K.

Table 1

Refined crystallographic data and reliability factors for the  $\text{La}_{0.6}\text{Sr}_{0.4}\text{MnO}_3$  nanoparticles. The nanoparticles size  $D$  are also presented.

Parameter	Calcination temperature			
	973 K	1073 K	1173 K	1273 K
$a$ (Å)	5.5005	5.4999	5.5028	5.5148
$c$ (Å)	13.3575	13.3367	13.3441	13.3586
$O(x)$	0.5493	0.5529	0.5415	0.5615
Volume (Å <sup>3</sup> )	350.00	349.37	349.94	351.85
$R_p$ (%)	10.2	11.0	11.4	9.3
$R_{wp}$ (%)	13.2	14.5	14.6	12.1
$R_F$ (%)	11.0	12.0	12.1	9.5
$\chi^2$	2.7	2.8	3.0	2.5
$D$ (nm)	$21 \pm 2$	$27 \pm 3$	$41 \pm 4$	$106 \pm 10$



**Fig. 2.** TEM micrograph of  $\text{La}_{0.6}\text{Sr}_{0.4}\text{MnO}_3$  samples annealed at temperatures of (a) 973 K, (b) 1073 K, (c) 1173 K and (d) 1273 K. The corresponding histogram of each sample is shown in the inset, where it is possible to see that the maximum is around to the obtained value by the X-ray diffraction technique.

sizes estimated from powder X-ray data are shown in Table 1. In order to confirm the average grain size, we used the TEM images shown in Fig. 2. It is possible to verify that the average nanograin size decreases from approximately 100 nm down to 20 nm for calcination temperatures from 1273 down to 973 K. These results show a very good agreement between the observed particle size from histogram (insets of Fig. 2) and the one from X-ray diffraction analysis. The TEM images also show that the particles (nanograins) exhibit a spherical morphology and that are slightly connected to each other. This information will be useful to our model, which will be presented further in Section 4.2.

## 4. Magnetic properties

### 4.1. Results

Magnetization curves as a function of applied magnetic field, at 4 K, are presented in Fig. 3 for all studied samples. It is possible to note that the magnetic saturation strongly depends on the nanoparticle size. The bulk sample has a magnetic saturation close to  $3.9 \mu_B$  and, considering the saturation as  $M^{\text{sat}} = g(0.6 \times 2 + 0.4 \times \frac{3}{2})\mu_B$ , we can estimate the Landé factor as  $g=2.17$  – a reasonable result for manganites when the quenching of the angular moments is not perfect and a really minor orbital contribution takes place [30]. On the other hand, for manganite nanoparticles, the magnetic saturation ranges from  $2.9 \mu_B$  (106 nm) down to  $2.1 \mu_B$  (21 nm). Considering this last case (21 nm), and the magnetic saturation  $M^{\text{sat}}$  written above, we would obtain  $g=1.16$  – a non-acceptable Landé factor for manganites. Thus, other mechanisms are reducing the magnetic

saturation of those nanoparticles by almost half. See Fig. 3 for further details.

In this direction, some works have already proposed a core-shell structure, with magnetic and non-magnetic coexistence [19,31]; and this idea is reasonable, but here we will propose an improvement. Any sample has a core and a surface; however, due to missing coordinate ions and some other strength on the surface, its magnetic arrangement is different from the core. The bulk sample has quite a small surface/core ratio and therefore the magnetic contribution from the distorted surface is negligible. On the other hand, nanoparticles have a much bigger surface/core ratio and thus the surface (shell) contribution must be taken into account. Thus, the model we will consider in the next sub-section refers to a core-shell problem, with a ferromagnetic core and a ferrimagnetic shell. Note that we propose a shell with a ferrimagnetic arrangement as the mechanism needed to reduce the magnetic saturation. We emphasize that the difference in the present model and the other proposed before [19] lies on the ferrimagnetic character of the shell, instead of non-magnetic. In addition, in order to support our choice (shell ferrimagnetic) we have to remember that the  $\text{La}_{1-x}\text{Sr}_x\text{MnO}_3$  system presents a very rich magnetic phase diagram [32] that depends on  $x$  amount. For  $x=0.4$  (studied sample) the material is supposed to be ferromagnetic at temperatures below  $T_C=320$  K, but any deviation of  $x=0.4$  (for either direction  $x > 0.4$  or  $x < 0.4$ ) can induce an antiferromagnetic arrangement. It is well known that nanoparticle surfaces have structural imperfections (for example, vacancies, defects and broken chemical bond) that change the surface composition in such a way that it modifies the magnetic interactions by localization of  $e_e$  electrons and causes different valences for Mn ions. These effects induce an antiferromagnetic phase in the shell, or

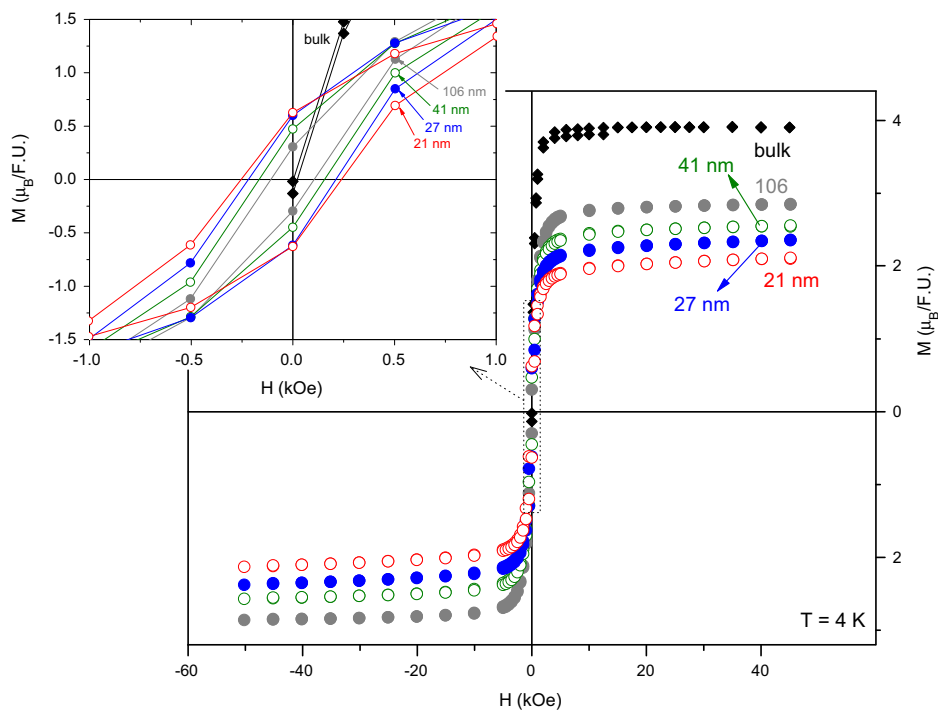


**Fig. 3.** Magnetization as a function of external magnetic field at 4 K. Note that the magnetic saturation strongly depends on the nanoparticle size. Inset: magnification at the origin, for low values of magnetic field. Note that bulk sample has no hysteresis, while, on the contrary, hysteresis is observed for all nanostructured manganites.

equivalently ferrimagnetic, since an uncompensated antiferromagnetic coupling gives a ferrimagnetic character.

Further on, the magnetization as a function of (low values of) magnetic field presents a hysteretic behavior for these nanoparticles, while the bulk sample is free of magnetic losses (see inset of Fig. 3). This is a common result [19] and it is due to the large surface anisotropy. Fig. 4 shows the magnetization as a function of temperature in an external magnetic field of 200 Oe. It is possible to see that the anisotropy also influenced  $M(T)$  curves, where a large irreversibility  $\Delta M$  at 4 K between the ZFC and the FC magnetization can be seen. Note in Fig. 5 that  $\Delta M$  decreases as the nanoparticles size increases (in order to include the bulk value we considered  $1/D$ , instead of  $D$ ). The bulk sample shows no irreversibility in the  $M(T)$  curves, as well as hysteresis in the  $M(H)$  isotherms.

On the other hand, the shape of the magnetization as a function of temperature curves also depends on the nanoparticle size. The bulk sample has an almost temperature independent behavior from low temperature up to the critical one, above which the magnetization suddenly drops to zero. Magnetization for nanoparticles is quite different, with a Brillouin-like shape. Note that the particle size does not change the critical temperature of the system that occurs ca. 320 K (obtained from the minimum on the first derivative of  $M(T)$ ). These results are in Fig. 4. The solid lines in Fig. 4 are fittings from the model, described in detail in the next section.

#### 4.2. The model

To further understand the magnetic behavior of those manganese nanoparticles, we considered a simple model based on a ferromagnetic core (since the bulk sample is ferromagnetic) and a ferrimagnetic shell (the unique way to justify those values of magnetic saturation – see Fig. 3 – otherwise the Landé factors would be close to one; absolutely unphysical for these manganites). See discussion in the previous subsection.

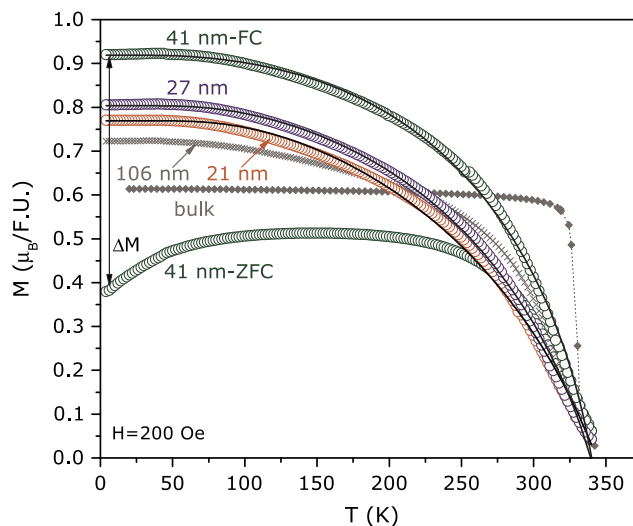


**Fig. 4.** Magnetization as a function of temperature with  $H=200$  Oe for all samples. Note the strong dependence of the magnetic behavior with nanoparticle size. Circles are experimental data and solid line are fittings of the model proposed in Section 4.2. Dotted line on the bulk sample is only a guide to the eyes. For the sake of clearness, only one ZFC curve is presented, but the irreversibility  $\Delta M$  at 4 K is presented in Fig. 5 for all samples.

Fig. 6 clarifies the proposed model, where the core has two sub-lattices ( $\text{Mn}^{3+}$  with  $s=2$  and  $3/5$  of molar fraction; and  $\text{Mn}^{4+}$  with  $s=3/2$  and  $2/5$  of molar fraction) aligned in a parallel fashion; and the shell has the same kind of two sub-lattices, however, aligned in an antiparallel way. Those spins interact through a mean-field, better described further in the text. We are considering the contact region between nanoparticles (nanograin boundaries) that presents the same magnetic arrangement as the free surface.

The total magnetization is given thus by

$$M = \rho M_{sh} + (1 - \rho) M_{co} \quad (2)$$

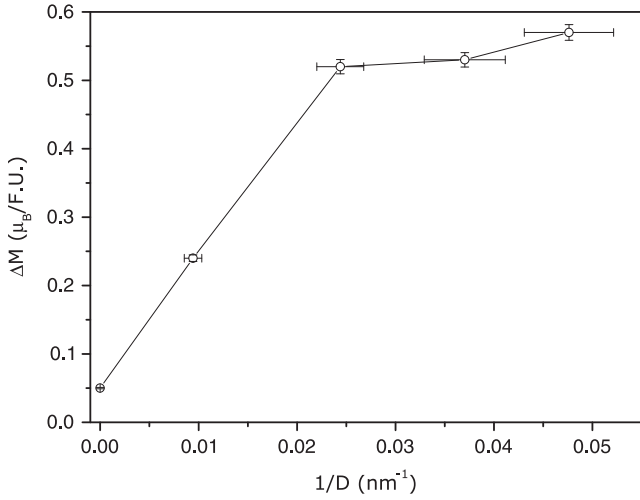


**Fig. 5.** Irreversibility between ZFC and FC magnetization at 4 K as a function of inverse nanoparticle diameter  $D$ .

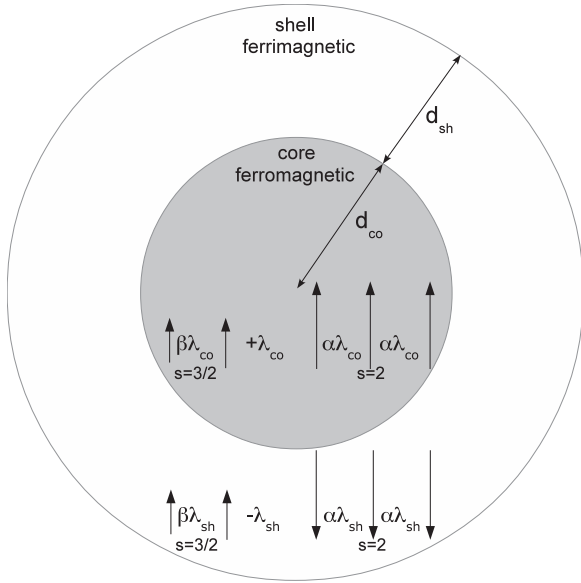


**Fig. 6.** Core-shell model. The core has a ferromagnetic character, while the shell is ferrimagnetic. Each one has two sub-lattices ( $\text{Mn}^{3+}$  and  $\text{Mn}^{4+}$ ) that interact through a mean-field (see Eq. (6)). Interactions strength and signals are also represented in this figure. In this figure the arrows (or vectors) represent the magnetic moment of ions  $\text{Mn}^{3+}$  ( $s=2$ ) and  $\text{Mn}^{4+}$  ( $s=3/2$ ).  $\beta\lambda$ 's describe the ferromagnetic interaction between  $\text{Mn}^{4+}$  ions into the core ( $\beta\lambda_{co}$ ) and into the shell ( $\beta\lambda_{sh}$ ), while  $\alpha\lambda$ 's represent ferromagnetic interaction between  $\text{Mn}^{3+}$  ions into the core ( $\alpha\lambda_{co}$ ) and into the shell ( $\alpha\lambda_{sh}$ ). The  $-\lambda_{sh}$  and  $+\lambda_{co}$  are associated to the mean field parameter of interaction between  $\text{Mn}^{3+}$  and  $\text{Mn}^{4+}$  sub-lattices in the shell (ferrimagnetic, negative sign) and core (ferromagnetic, positive sign), respectively.

where  $0 < \rho < 1$  is the shell magnetization fraction. The shell and core contributions depend on the  $s=2$  and  $s=3/2$  sub-lattices:

$$M_{sh,co} = M_{sh,co}^{(2)} + M_{sh,co}^{(3/2)} \quad (3)$$

The above notation means that this equation holds for both shell and core. Sub-lattice magnetizations therefore need to be defined and we considered for this purpose

$$M_{sh,co}^{(s)} = N^{(s)} g_{sh,co} S \mu_B \mathcal{B}[\chi_{sh,co}^{(s)}] \quad (4)$$

where  $\mathcal{B}[y]$  is the standard Brillouin function [30],  $N^{(2)} = 3/5$  and  $N^{(3/2)} = 2/5$ . In addition

$$\chi_{sh,co}^{(s)} = g_{sh,co} S \frac{\mu_B \mathcal{B}^{(s)}_{sh,co}}{k_B T} \quad (5)$$

where  $\mathcal{B}_{sh,co}^{(s)}$  is the mean-field term, given by

$$\begin{pmatrix} \mathcal{B}_{sh,co}^{(3/2)} \\ \mathcal{B}_{sh,co}^{(2)} \end{pmatrix} = B_0 + \lambda_{sh,co} \begin{pmatrix} \beta & \sigma_{sh,co} \\ \sigma_{sh,co} & \alpha \end{pmatrix} \begin{pmatrix} M_{sh,co}^{(3/2)} \\ M_{sh,co}^{(2)} \end{pmatrix} \quad (6)$$

where  $\sigma_{sh} = -1$  and  $\sigma_{co} = +1$ .

In accordance with Fig. 6 and the above equation,  $s=2$  spins into the core/shell interact via  $\alpha\lambda_{sh,co}$ , while  $s=3/2$  spins into the core/shell interact via  $\beta\lambda_{sh,co}$ . The difference between the ferri- and ferromagnetic arrangements lies on the  $s=2$  and  $s=3/2$  interactions, i.e.,  $+\lambda_{co}$  into the core and  $-\lambda_{sh}$  into the shell. Finally, we consider that the interaction between core and shell is negligible, since it occurs, in principle, on the interface – with much less spins than in the volume. It is a well-known self-consistent problem, since the magnetizations on the right-hand side of Eq. (6) depend themselves on the left-hand side of Eq. (4) – for both shell and core. The solution is only obtained numerically.

#### 4.3. Discussion

The model proposed previously was fitted to the experimental data with some free parameters:  $g_{sh}$ ,  $g_{co}$ ,  $\alpha$ ,  $\beta$  and  $\rho$ . The model, as discussed above, is based on the missing coordinate ions on surface and, consequently, extra strength on those surface ions promoting therefore a shell, with different magnetic properties from the core. In other words, these differences lie on the structure and, consequently, on the magnetic properties (magnetic interactions and Landé factor). In this sense, it is reasonable to consider different Landé factors and different kinds of interaction  $\lambda_{co}$  and  $\lambda_{sh}$  for core and shell, respectively.

The fittings of the model on the experimental data are in Fig. 4 and the good theoretical-experimental agreement is presented – solid line (theoretical) on the circles (experimental). Note, however, an important point:  $M(T)$  of the sample with 106 nm nanoparticles has not a fitting, due to the worse quality of the theoretical-experimental agreement. We understand these results: our model considers single-domain particles (and thus works for the smaller nanoparticles); and increasing the nanoparticle size, magnetic domains appears and the model loses validity. Indeed,  $M(T)$  of 106 nm nanoparticle does not follow the tendency of the other nanoparticles and starts to approach to the bulk behavior, that, on its turn, has magnetic domains. Some works [33] also propose that the single-/multi-domain crossover lies close to 70 nm.

Optimized parameters of the fittings on the single magnetic domain nanoparticles (smaller than 41 nm) are in Fig. 7. The Landé factor for the core,  $g_{co}$ , has a minor deviation from the bulk value, while  $g_{sh}$  approaches to 2 decreasing the nanoparticle diameter. See Fig. 7-top. Also in this panel, we presented the core-shell ratio  $\rho$ , in accordance with Eq. (2), i.e.,  $\rho$  means the magnetic fraction from the shell – and it is found to be independent of the nanoparticle diameter; but note, at least for this range of nanoparticle diameters (from 21 nm up to 41 nm).

From the obtained  $\rho$  and Landé factors we can estimate the magnetic saturation:  $M^{sat} = \rho M_{sh}^{sat} + (1-\rho) M_{co}^{sat}$ , where  $M_{sh}^{sat} = (0.6 \times 2 - 0.4 \times \frac{3}{2}) g_{sh}$  and  $M_{co}^{sat} = (0.6 \times 2 + 0.4 \times \frac{3}{2}) g_{co}$ . Thus, the optimized parameters on this equation lead to the values in Fig. 7-bottom (presented as °). There is a good agreement between the estimated and experimental magnetic saturations, ratifying the validity of the proposed model. Since we considered the shell not fully oriented, a true saturation of these nanoparticles is expected for much higher

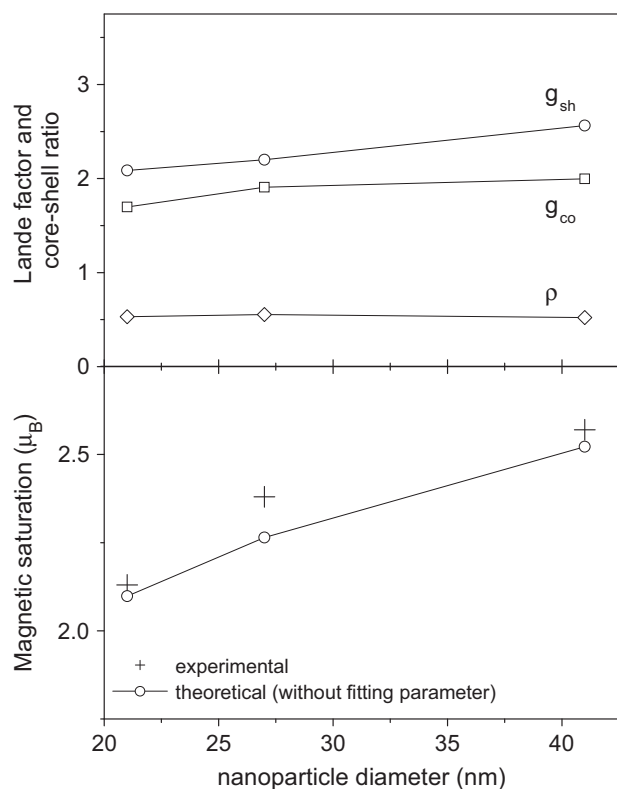


**Fig. 7.** Optimized parameters from the fitting of the model (see Section 4.2), to the experimental  $M(T)$  curves in Fig. 4. Top panel: Landé factors and core-shell ratio. Bottom panel: experimental and estimated (without fitting) magnetic saturation. See text for further details.

values of magnetic field, in order to reach  $M^{sat} = \rho 1.8g_{sh} + (1 - \rho)1.8g_{co}$ .

## 5. Conclusions

From standard sol-gel techniques we produced  $\text{La}_{0.6}\text{Sr}_{0.4}\text{MnO}_3$  nanoparticles by controlling the annealing temperature. From the X-ray diffraction and the Scherrer equation we obtained the nanoparticle size that ranges from 21 nm up to 106 nm; and these values were confirmed from transmission electron microscopy. Magnetization measurements show that those nanoparticles have a remarkable different behavior. In order to understand these differences, we developed a theoretical model based on a core(ferromagnetic)-shell(ferrimagnetic) pattern, and an excellent agreement was obtained. We found, based on this theoretical model, that the critical nanoparticle size below which the system behaves like a single domain is close to 40 nm. In addition, this successful model has important outputs, like the Landé factor and the core/shell magnetization factor. Finally, the model indicates that the shell has a ferrimagnetic character, instead of “non-magnetic” or “magnetically dead” as claimed by some works [24,19].

## Acknowledgments

We acknowledge FAPERJ, CAPES, CNPq and PROPPI-UFF for financial support.

*Author contributions:* R.J.C.-V., V.M.A., S.S.P. and D.L.R.: sample preparation, X-ray analysis; M.S.R. and T. C.-S.: Theoretical model; A.P.C.C. and D.L.R.: TEM measurements and analysis; A.A.C.: magnetic measurements. All authors discussed results and contributed to write the text of this paper.

## References

- [1] D. Zhang, K.J. Klabunde, C.M. Sorensen, G.C. Hadjipanayis, *Phys. Rev. B* 58 (2006) 14167.
- [2] O. Kaman, E. Pollert, P. Veverka, M. Veverka, E. Hadova, K. Knizek, M. Marysko, P. Kaspar, M. Klementova, V. Grunwaldova, S. Vasseur, R. Epherre, S. Mornet, G. Goglio, E. Duguët, *Nanotechnology* 20 (2009) 275610.
- [3] S. Chono, S.-D. Li, C.C. Conwell, L. Huang, *J. Control. Release* 131 (2008) 64.
- [4] X.-J. Hu, J.-K. Liu, Y. Mu, *Mater. Lett.* 62 (2008) 3824.
- [5] J. Liu, Z. Zhao, J. Wang, C. Xu, A. Duan, G. Jiang, Q. Yang, *Appl. Catal. B* 84 (2008) 185.
- [6] S.P. Mathew, S.N. Kaul, *Appl. Phys. Lett.* 98 (2011) 172505.
- [7] T. Zhu, B.G. Shen, J.R. Sun, H.W. Zhao, W.S. Zhan, *Appl. Phys. Lett.* 78 (2001) 3863.
- [8] P. Dey, T.K. Nath, P.K. Manna, S.M. Yusuf, *J. Appl. Phys.* 104 (2008) 103907.
- [9] P. Katiyar, D. Kumar, T.K. Nath, A.V. Kvit, J. Narayan, R.K. Singh, *Appl. Phys. Lett.* 79 (2001) 1327.
- [10] M. Vasilakaki, K.N. Trohidou, *Phys. Rev. B* 79 (2009) 144402.
- [11] C. Westman, S. Jang, C. Kim, S. He, G. Harmon, N. Miller, B. Graves, N. Poudyal, R. Sabirianov, H. Zeng, M. DeMarco, J.P. Liu, *J. Phys.: D: Appl. Phys.* 41 (2008) 225003.
- [12] R. Kodama, *J. Magn. Magn. Mater.* 200 (1999) 359–372.
- [13] X. Battle, A. Labarta, *J. Phys. D: Appl. Phys.* 35 (2002) R15.
- [14] T. Ogasawara, K. Ohgushi, Y. Tomioka, K.S. Takahashi, H. Okamoto, M. Kawasaki, Y. Tokura, *Phys. Rev. Lett.* 94 (2005) 087202.
- [15] D.L. Rocco, A.A. Coelho, S. Gama, M.C. Santos, *J. Appl. Phys.* 113 (2013) 113907.
- [16] S. Jin, T.H. Tiefel, M. McCormack, R.A. Fastnacht, R. Ramesh, L.H. Chen, *Science* 264 (1994) 413.
- [17] R.E. Dinnebier, S.J.L. Billinge, in: Y. Tokura (Ed.), *Colossal Magnetoresistive Oxides*, Gordon and Breach, 2000.
- [18] P. Lampen, N.S. Bingham, M.H. Phan, H. Kim, M. Osofsky, A. Piqué, T.L. Phan, S. C. Yu, H. Srikanth, *Appl. Phys. Lett.* 102 (2013) 062414.
- [19] S.B. Xi, W.J. Lu, H.Y. Wu, P. Tong, Y.P. Sun, *J. Appl. Phys.* 112 (2012) 123903.
- [20] A. Rostamnejadi, H. Salamati, P. Kameli, *J. Supercond. Nov. Magn.* 25 (2012) 1123.
- [21] L.E. Hueso, P. Sande, D.R. Miguens, J. Rivas, F. Rivadull, *J. Appl. Phys.* 91 (2002) 1215.
- [22] A. Rostamnejadi, M. Venkatesan, J. Alaria, M. Boese, P. Kameli, H. Salamati, J.M. D. Coey, *J. Appl. Phys.* 110 (2011) 043905.
- [23] W. Tang, W.J. Lu, X. Luo, B.S. Wang, X.B. Zhu, W.H. Song, Z.R. Yang, Y.P. Sun, *J. Magn. Magn. Mater.* 322 (2010) 2360.
- [24] S. Xi, W. Lu, Y. Sun, *J. Appl. Phys.* 111 (2012) 63922.
- [25] C.H. Shen, C.C. Chen, R.S. Liu, R. Gundakaram, S.F. Hu, J.M. Chen, *J. Solid State Chem.* 156 (2001) 117–121.
- [26] J. Rodriguez-Carvajal, *An Introduction to the program FullProf 2000* (version July 2001), 2001.
- [27] R.E. Dinnebier, S.J.L. Billinge, *Powder Diffraction—Theory and Practice*, PRS Publishing, 2008.
- [28] P. Dey, T.K. Nath, *Phys. Rev. B* 73 (2006) 214425.
- [29] W.J. Lu, X. Luo, C.Y. Hao, W.H. Song, Y.P. Sun, *J. Appl. Phys.* 104 (2008) 113908.
- [30] M. Reis, *Fundamentals of Magnetism*, Elsevier, San Diego, USA, 2013.
- [31] R. Bhowmik, *J. Magn. Magn. Mater.* 323 (2011) 311–315.
- [32] A. Szewczyk, M. Gutowska, B. Dabrowski, *Phys. Rev. B* 72 (2005) 224429.
- [33] S.B. Xi, W.J. Lu, H.Y. Wu, P. Tong, Y.P. Sun, *J. Appl. Phys.* 112 (2012) 124307.